crystals

MDPI

Article

Lattice Anharmonicity and Grüneisen Parameter Estimation Using X-Ray Diffraction

Sheetal Jain, Aditya Chugh and Young-June Kim *

Department of Physics, University of Toronto, Toronto, ON M5S 1A7, Canada
* Correspondence: youngjune.kim@utoronto.ca

Abstract

Powder X-ray diffraction measurements were carried out on various samples to characterize their thermal expansion over a wide temperature range (93–1373 K). Using an effective interatomic potential model, we present a method to empirically estimate the Grüneisen parameter, as well as cubic and quartic anharmonic contributions to the lattice potential. This method is further tested on materials for which thermal expansion data are readily available. For most of the materials surveyed, the Grüneisen parameter values match those reported in the literature, obtained using traditional techniques. Thus, this work presents a novel and convenient Grüneisen parameter estimation method that uses measurements of only one physical property, thermal expansion.

Keywords: Grüneisen parameter; thermal expansion; lattice anharmonicity; X-ray diffraction

1. Introduction

Lattice anharmonicity is crucial for understanding many physical properties of solids, such as thermal expansion and thermal conductivity. A purely harmonic crystal would exhibit no thermal expansion and infinite lattice thermal conductivity at absolute zero temperature [1]. Therefore, a good understanding of the lattice anharmonicity of various materials is important not only to explain their thermodynamic and thermal transport properties but also to predict and understand their functional applications.

For example, good thermoelectric materials have low lattice thermal conductivity and high electrical conductivity. Since lowering the electronic thermal conductivity inevitably reduces electrical conductivity, materials with intrinsically low lattice thermal conductivity are desirable for thermoelectric applications. Since anharmonicity lowers lattice thermal conductivity, highly anharmonic materials are very good candidates for thermoelectric materials. Thus, finding a quick way to estimate the lattice anharmonicity in various materials would be very useful for thermoelectric materials research [2].

Moreover, lattice anharmonicity is important in explaining anomalous thermal transport properties, such as the thermal Hall effect [3–7]. Four-phonon interactions were suggested to be responsible for the observed thermal Hall effect in $SrTiO_3$ [3], which could directly arise from quartic anharmonicity in interatomic interactions [6]. Therefore, understanding and estimating anharmonicity may be the key to unraveling the mystery behind the phonon thermal Hall effect as well.

However, quantifying the anharmonic lattice potential is non-trivial and computationally expensive. Traditionally, the dimensionless Grüneisen parameter γ is considered a

Check for updates

Academic Editor: Volodymyr Bon

Received: 6 January 2026
Revised: 29 January 2026
Accepted: 30 January 2026
Published: 6 February 2026

Copyright: © 2026 by the authors. Licensee MDPI, Basel, Switzerland. This article is an open access article distributed under the terms and conditions of the Creative Commons Attribution (CC BY) license.

measure of 'overall' anharmonicity in a material. In quasi-harmonic approximation, its value at room temperature ($T = 298$ K), γ_0, is given as

$$\gamma_0 = \frac{\alpha_V V_m B_T}{C_V}, \quad (1)$$

where α_V is the volumetric thermal expansion coefficient, V_m is the molar volume, B_T is the isothermal bulk modulus, and C_V is the isochoric molar specific heat capacity, with all values being at room temperature. This thermodynamic quantity is often estimated using first-principles approaches that compute mode-resolved Grüneisen parameters from phonon frequencies [8–10]. A recent study also demonstrated that the Grüneisen parameter can be extracted semi-empirically using the bond valence method [11,12]. On the other hand, purely empirical determination of the Grüneisen parameter typically relies on Equation (1), which requires measurements of four separate physical quantities of a material.

Due to the experimental complexity of measuring multiple physical properties, several alternative approaches have been explored to estimate the Grüneisen parameter [13]. One of them is to measure the transverse (v_t) and longitudinal (v_l) sound speeds of the material, and then determine the Grüneisen parameter using the relation to Poisson's ratio (ν_p) [14–16]:

$$\gamma_0 = \frac{3}{2}\left(\frac{1+\nu_p}{2-3\,\nu_p}\right), \quad (2)$$

where $\nu_p = (1 - 2\,(v_t/v_l)^2)/(2 - 2\,(v_t/v_l)^2)$. The measurement of transverse and longitudinal sound speeds requires a single crystal sample, which is usually significantly more difficult to prepare than a powder sample. Using a powder sample results in a larger error bar for Poisson's ratio [16], making it difficult to determine the Grüneisen parameter with high accuracy.

Another method to obtain information about anharmonic lattice potential is the cumulant analysis of extended X-ray absorption fine structure (EXAFS) spectra. The anharmonic contribution to thermal vibration of average atomic position can be captured by fitting the phase difference and amplitude ratio, which provide cubic and quartic anharmonicity, respectively [17–20]. The Grüneisen parameter can also be estimated directly from the EXAFS spectra [21,22], but this technique is not widely used, due to the complexity of data analysis and processing.

Alternatively, since thermal expansion is purely an anharmonic effect, anharmonicity could be modelled based on thermal expansion data, as illustrated in the dilatometry study [23]. We extend this idea further by developing a method to estimate the Grüneisen parameter based on thermal expansion data obtained with powder X-ray diffraction, an easily accessible experimental tool. We develop an effective potential model in the next section, similar to that employed in Ref. [23]. By fitting this model to thermal expansion data, both the Grüneisen parameter and interatomic effective potential coefficients can be estimated. An experimental test of this method has been carried out for 60 different materials, using both existing and new data. We demonstrate that this method of estimating the Grüneisen parameter works well for most materials tested, with only a few exceptions. We also discuss possible reasons for the discrepancy.

This thermal expansion method for estimating the Grüneisen parameter would be particularly useful when measurements are performed under extreme conditions, such as high temperature and high pressure, where measuring multiple properties to determine the Grüneisen parameter would be significantly more challenging.

2. Experimental Section

All powder X-ray diffraction measurements were carried out on a Rigaku Smartlab® X-ray diffractometer. Cu K-α X-ray radiation was used in the measurements, with the powder samples mounted in the Bragg–Brentano reflection geometry. Anton-Paar DHS and DCS temperature stages were used for heating and cooling from room temperature (298 K), respectively. The samples were kept in a vacuum during the X-ray diffraction measurements. Commercial powder samples were used in the measurements, except for BiCuSeO, La_2CuO_4, and $La_{1.85}Sr_{0.15}CuO_4$, which were prepared using typical solid-state synthesis methods [24,25]. All powder samples were hand-ground in a mortar and pestle before the powder XRD measurements. The loose powder samples were then placed in a dish-type sample holder.

3. Anharmonicity Modelling

For simplicity, we consider a one-dimensional anharmonic potential of the form $\phi = cx^2 - gx^3 - fx^4$. The significance of these terms is shown graphically in Figure 1. In Figure 1a, a purely harmonic effective potential is considered. As temperature increases, higher-energy states become thermally populated, but the mean atomic position within the effective potential does not change, as indicated by the solid red dots. Cubic anharmonicity introduces asymmetry in the lattice potential, and the mean atomic position shifts with increasing energy state, indicating a linear thermal expansion, as shown by the red trend line in panel (b). Furthermore, the addition of quartic anharmonicity to the effective potential leads to non-linear thermal expansion, as shown in panel (c). Thus, linear thermal expansion at low temperatures is a measure of the cubic anharmonicity, while the relative deviation of this linear trend at high temperatures is proportional to the quartic anharmonicity.

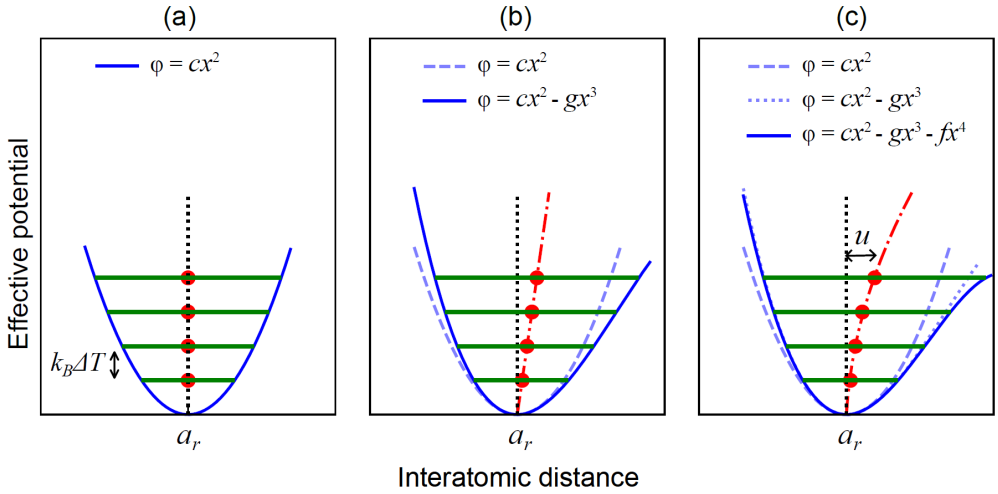


Figure 1. A heuristic diagram illustrating the effect of anharmonicity on thermal expansion. (**a**) Purely harmonic potential; (**b**) a cubic term added; (**c**) a quartic term added. For each panel, the positions of the red dots represent the average interatomic distance $\langle x \rangle_T$ in Equation (3), and the progression from the bottom rung to the top rung represents increasing temperature and the resulting thermal energy. The purely harmonic effective potential shows no thermal expansion; the introduction of cubic anharmonicity leads to linear thermal expansion; further, the addition of quartic anharmonicity is needed to produce non-linear thermal expansion.

This qualitative discussion can be formalized using the semi-classical treatment of thermal expansion developed by Mukherjee et al. [23] using the lattice potential ϕ given above. The average thermal displacement in interatomic distance $\langle x \rangle_T$ is found to be

$$\langle x \rangle_T = \frac{3}{4} g_1 a_r \epsilon [1 - G\epsilon - F\epsilon^2], \tag{3}$$

where $G = \frac{15}{16} g_2 - 8 f_1$, $F = \frac{35}{16}\left(\frac{15}{4} g_2 f_1 + 3(f_1)^2\right)$, and the reduced effective potential coefficients (g_1, f_1, g_2) are $g_1 = g/c^2 a_r$, $f_1 = f/c^2$, and $g_2 = g^2/c^3$. Here, a_r is the lattice constant at the reference temperature T_r. Detailed derivation can be found in Appendix A.

Since we are modelling thermal expansion over a wide temperature range, it is important to note that anharmonic deviations are more significant at higher temperatures. Thus, we focus on the high-temperature region and assume $\epsilon \approx k_B T$. Note that $\langle x \rangle_T$ is proportional to g/c^2, meaning that cubic anharmonicity is required for non-zero thermal displacement as shown in Figure 1. In addition, both G and F depend strongly on f, which indicates that quartic anharmonicity is mostly responsible for the deviation in T-linear behaviour of $\langle x \rangle_T$.

Relative thermal expansion ($\Delta a/a_r$) with respect to a reference temperature can be written as

$$\frac{\Delta a}{a_r} = \frac{\langle x \rangle_T - \langle x \rangle_{T_r}}{a_r} = b_1 \Big[(T - T_r) - b_2 (T^2 - T_r^2) - b_3 (T^3 - T_r^3) \Big], \tag{4}$$

which can be used to fit thermal expansion data. The fitting parameters, b_1, b_2, and b_3, can then be used to estimate the anharmonic effective potential coefficients c, f, and g (see Appendix B). Furthermore, the effective model discussed above can be directly connected to the average Grüneisen parameter at room temperature, γ_0. Using the Mie–Grüneisen equations of state, γ_0 is calculated in terms of the effective potential [22,26–29]:

$$\gamma_0 = -\frac{a_0}{6}\left[\frac{\phi'''(u)}{\phi''(u)}\right] = \frac{a_0}{6}\left[\frac{3g + 12fu}{c - 3gu - 6fu^2}\right], \tag{5}$$

where a_0 and $u = \langle x \rangle_0$ are the lattice constant and mean thermal displacement at room temperature, respectively. Note that Equation (5) is derived under the assumption that only nearest neighbours contribute to the effective potential, making this an inherently short-range model. See Appendix C for the derivation of Equation (5).

We note that the present approach intentionally uses a minimal model that maps the full three-dimensional lattice dynamics onto a one-dimensional effective coordinate associated with the average change in interatomic separation. The key assumptions are as follows:

- Isotropic averaging: We use the unit-cell volume (expressed as an equivalent cubic edge length) to represent an average linear expansion, thereby targeting an average Grüneisen parameter rather than direction-resolved values.
- Thermal averaging approximation: The model uses a high-temperature approximation for thermal energy in the averaging procedure, prioritizing an accurate description at high temperatures where anharmonic contributions are most pronounced.
- Short-range interaction limit: The Mie–Grüneisen relation used to obtain Equation (5) is derived under an effective nearest-neighbour picture; thus, materials with substantial long-range interactions (e.g., highly polar lattices with large dielectric response, strong electron–phonon coupling, soft-mode dominated dynamics) may show systematic deviations.

Consequently, the method is expected to perform best for materials with moderate anisotropy and predominantly short-to-intermediate range bonding, and it should be applied with caution in systems exhibiting strong long-range electrostatics or pronounced anisotropy.

4. Results

Experimentally, we measure thermal expansion using temperature-dependent powder X-ray diffraction (XRD). These measurements yield the behaviour of lattice constants (and unit cell volume) as a function of temperature. The relative thermal expansion can then be calculated as $(a(T) - a_r)/a_r$, where $a(T)$ is the lattice constant at temperature T, and a_r is the lattice constant at the lowest measured temperature T_r (typically 93 K in this study), used as a reference for quantifying the thermal expansion. Here, a is simply the lattice constant in the case of cubic lattices. In order to make this comparable for non-cubic lattices, a is evaluated as $\sqrt[3]{V}$, where V is the unit cell volume. This allows for direct comparison of the relative thermal expansion of these materials with different lattice types.

The thermal expansion data from lattice constants is presented in Figure 2. The solid lines are fits to Equation (4). The thermal expansion slope at low temperatures is found to be large for NaBr, PbTe, and Bi_2Te_3. These materials would be expected to have large relative cubic anharmonicities (g/c^2). On the other hand, the relative deviation from the low-temperature slope at higher temperatures is largest for NaBr and BiCuSeO, which would correspondingly have larger relative quartic anharmonicities (f/c^2). It is also noted that the lattice structure plays an important role in thermal expansion. Hexagonal and cubic BN have the same B-N bond, but the different lattice structures lead to quite distinct thermal expansion behaviour as shown in Figure 2. The copper oxide superconductors (La_2CuO_4 and $La_{1.85}Sr_{0.15}CuO_4$), on the other hand, are nearly iso-structural, and indeed show similar relative thermal expansion behaviour regardless of doping.

The obtained thermal expansion coefficients (b_1, b_2, and b_3) from these fits are then used to estimate the coefficients of the effective potential (c, f, and g) using Equation (A3). All these values are tabulated in Tables 1 and 2. The fits yield goodness-of-fit parameters, and reduced χ^2 close to 1 for all materials.

With so-obtained effective potential coefficients, the values of the average Grüneisen parameter can be estimated, using Equation (5). That is, we determined the average Grüneisen parameter based solely on the thermal expansion data. These values, for the various materials measured, are also tabulated in Table 2. These Grüneisen parameter values also agree with those found in the literature for most materials, also shown in the last two columns of Table 2.

Table 1. Thermal expansion coefficients (b_1, b_2, and b_3) as well as temperature range for thermal expansion measurements, for all materials of interest.

Sample	b_1 ($\times 10^{-6}$ K^{-1})	b_2 (K^{-1})	b_3 (K^{-2})	Temp. Range (K)
BiCuSeO	6.8 (7)	$-1.0\ (2) \times 10^{-2}$	$1.1\ (3) \times 10^{-5}$	93–1073
PbTe	12 (2)	$3.6\ (4) \times 10^{-3}$	$-6.5\ (7) \times 10^{-7}$	93–773
Bi_2Te_3	11 (3)	$5.2\ (6) \times 10^{-3}$	$-1.4\ (3) \times 10^{-6}$	93–673
NaBr	18 (3)	$1.2\ (2) \times 10^{-3}$	$1.8\ (3) \times 10^{-5}$	93–773
Si	3.6 (4)	$2.0\ (2) \times 10^{-4}$	$5.3\ (6) \times 10^{-9}$	93–1373
NiO	10.0 (9)	$-8.8\ (9) \times 10^{-3}$	$8.3\ (9) \times 10^{-6}$	93–1373
hexagonal BN	7.0 (7)	$-7.7\ (8) \times 10^{-4}$	$6.2\ (7) \times 10^{-8}$	93–1373
cubic BN	0.71 (9)	$-2.7\ (4) \times 10^{-6}$	$9.5\ (9) \times 10^{-12}$	93–1373
La_2CuO_4	5.3 (5)	$5.6\ (4) \times 10^{-4}$	$1.5\ (2) \times 10^{-8}$	93–1273
$La_{1.85}Sr_{0.15}CuO_4$	5.9 (6)	$6.3\ (6) \times 10^{-4}$	$2.5\ (2) \times 10^{-8}$	93–1273

Table 2. Effective potential coefficients (c, g, f), average Grüneisen parameter at room temperature, γ_0, as well as its reference values, for all materials of interest.

Sample	c (eV Å^{-2})	g (eV Å^{-3})	f (eV Å^{-1})	γ_0	Ref. Value	Source
BiCuSeO	0.80 (3)	0.26 (1)	9.3 (4)	1.49 (5)	1.5 (1)	[16]
PbTe	1.4 (1)	2.2 (1)	−9.6 (4)	2.00 (8)	2.1 (1)	[30,31]
Bi_2Te_3	0.88 (4)	2.6 (2)	−5.6 (3)	1.50 (5)	1.5 (1)	[32]
NaBr	2.9 (1)	1.4 (1)	1.6 (1)	2.21 (9)	2.3 (1)	[33]
Si	0.58 (5)	0.10 (5)	0.10 (5)	0.48 (3)	0.45 (5)	[34]
NiO	0.61 (5)	0.24 (3)	4.8 (4)	1.86 (7)	1.8 (1)	[35]
hexagonal BN	0.30 (5)	0.024 (6)	0.10 (1)	0.11 (1)	0.10 (5)	[36]
cubic BN	13 (1)	6.4 (3)	1.0 (2)	0.92 (4)	0.95 (8)	[36]
La_2CuO_4	1.6 (1)	1.0 (1)	−1.8 (2)	1.69 (6)	3.8	[37]
$La_{1.85}Sr_{0.15}CuO_4$	0.98 (7)	0.47 (5)	−0.85 (7)	1.15 (4)	3.2	[37]

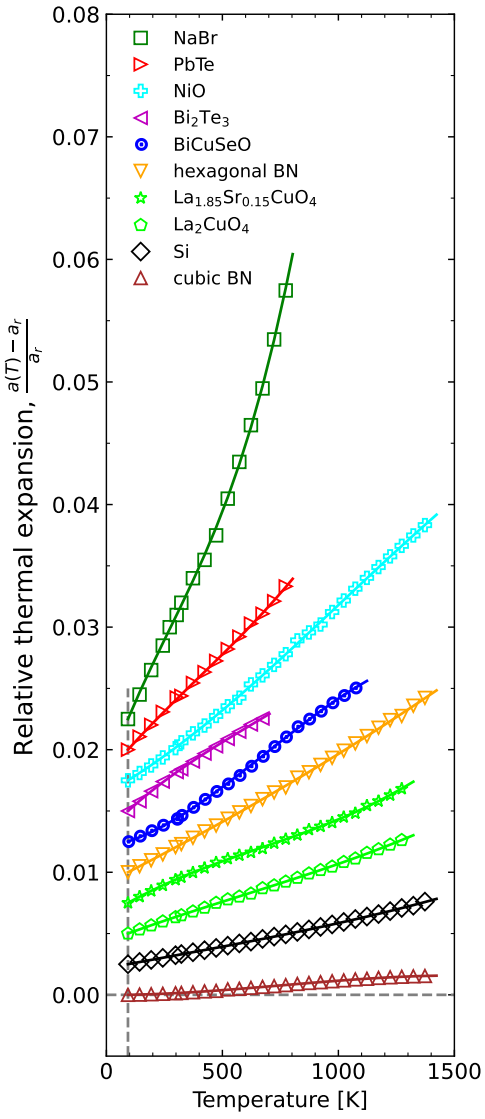


Figure 2. Relative thermal expansion, experimentally determined from powder XRD as a function of temperature for the materials of interest. The solid lines represent the anharmonic fits for non-linear thermal expansion, Equation (4). These fits match the data well across the entire temperature range. Note that the data and fits are offset along the y-direction for each material for visual clarity. The horizontal and vertical dashed lines are reference lines indicating zero thermal expansion and the base temperature, respectively.

In Figure 3, the comparison of the Grüneisen parameter obtained using two different methods is shown for various materials. The horizontal axis values are the Grüneisen parameters extracted using only thermal expansion, using Equation (5). The vertical axis values are from traditional measurements found in the literature, for example, using Equation (1). The dashed black line represents the perfect match between the Grüneisen parameter extracted from this work and the values found in the literature. Of the 10 materials measured in the current study, eight are found to lie on the dashed line, indicating that the Grüneisen parameter agrees with the previous literature within the error bar. Only layered copper oxides (La_2CuO_4 and $La_{1.85}Sr_{0.15}CuO_4$) show significant deviations.

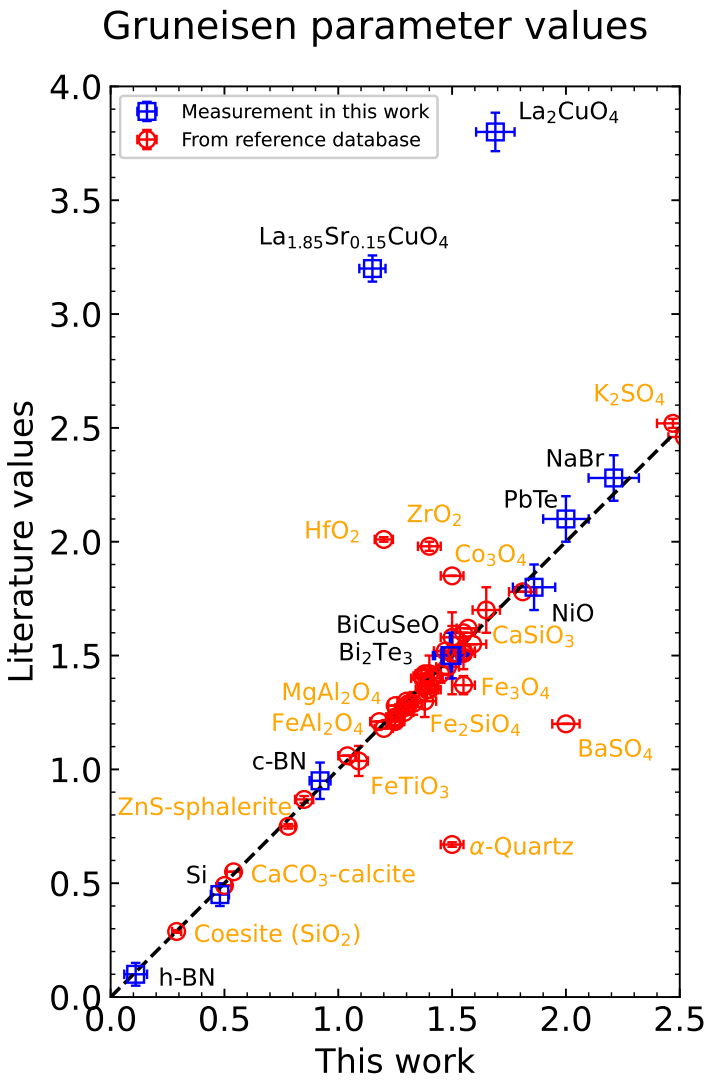


Figure 3. Comparison of Grüneisen parameters found in this work, using thermal expansion (horizontal axis), against values found in the literature (vertical axis). The blue squares are materials whose thermal expansion was measured by powder XRD in this study, while the red circles are those extracted from existing data found in references [38–72]. The dashed black line is drawn to denote a perfect match between the two. For the full list of materials and data, see Supplementary Materials.

In order to test the validity of this procedure beyond the materials studied here, we gathered information on many additional materials from the literature. For structural data, we use the thermal expansion coefficients for various materials compiled in Ref. [38]. Most of these materials are common geological ceramics, including transition metal oxides, carbonates, sulphates, and silicates. Using the same procedure described above, the Grüneisen

parameter of these materials was extracted from the thermal expansion data. These values are compared with those reported in the literature. These results are also shown in Figure 3, in red circles (see Supplementary Material for the data). Out of the 50 additional materials examined, 44 are found to agree within the error bar. Notable outliers are discussed below. These findings suggest that the thermal expansion model described in this work is a convenient empirical method to estimate the Grüneisen parameter of most materials, with some caveats to be discussed in the next section.

5. Discussion

Most materials (52 out of 60) studied in Figure 3 show fairly good agreement, within error bars, between estimates of the Grüneisen parameter using thermal expansion in this work, and values from the literature. This level of good agreement is somewhat surprising, given the simplicity of the modelling and the variety of materials reported in Figure 3. Many of the materials that show good agreement are not cubic, and some have a layered structure. The notable exceptions are the cuprates HfO_2, ZrO_2, Co_3O_4, $BaSO_4$, and α-Quartz.

It is worth noting that HfO_2 ($\kappa \sim 26$) [73], ZrO_2 ($\kappa \sim 32$) [74], Co_3O_4 ($\kappa \sim 11$) [75], and $BaSO_4$ ($\kappa \sim 11$) [76] exhibit unusually large dielectric constants [77]. These large dielectric constants may indicate long-range interactions within the lattice constants [78] and lattice [77]. For cuprates, too, it has been suggested that long-range interactions may play a significant role in lattice dynamics [79]. Note again that the Mie–Grüneisen relation used to obtain Equation (5) is derived under an effective nearest-neighbour picture, making the procedure used to estimate the Grüneisen parameter in this work inherently a short-range model. The short-range assumption could be relaxed by incorporating additional coordination shells in an effective potential, so that Equation (5) is generalized beyond a purely nearest-neighbour picture.

Despite using an isotropic, one-dimensional, simplified effective potential, the model accurately estimates the Grüneisen parameter for most materials. For cubic materials with approximately isotropic lattice properties, such one-dimensional modelling is perhaps justified. However, the good agreement for a large number of anisotropic materials is a surprising finding in this study. For non-cubic lattices, we use the unit-cell volume to define an equivalent cubic edge length $a_{\mathrm{eq}} = V^{1/3}$. This volumetric averaging is consistent with the fact that the Grüneisen parameter is expressed in volume-dependent quantities. In strongly anisotropic crystals, however, axis-dependent expansion and mode anisotropy can introduce systematic error; in particular, compensating positive or negative expansions along different axes may yield a small net change in volume even when some phonon branches are highly anharmonic. We note that several anisotropic materials, such as cuprates and α-quartz, exhibit large deviations, underscoring the shortcomings of the isotropic effective model used here. For these cases, it may be possible to improve the agreement by fitting the thermal expansion of individual lattice parameters to obtain direction-resolved "effective Grüneisen" parameters.

In addition to providing a more straightforward method of determining the Grüneisen parameter, the thermal expansion model also allows us to estimate the cubic and quartic anharmonic contributions separately. While the Grüneisen parameter estimates the overall combined anharmonicity in a material, this single parameter is unable to distinguish between cubic and quartic anharmonicity. Knowledge of cubic and quartic anharmonic contributions allows one to assess a material's applicability for its anharmonic properties in different temperature ranges, since cubic anharmonicity shows a significant impact at lower temperatures, while effects of quartic anharmonicity are more pronounced at higher temperatures, as shown in Figure 1.

To further illustrate this, we consider Bi_2Te_3 and BiCuSeO. Both have the same value of the Grüneisen parameter, 1.5, as shown in Table 1. However, their thermal expansion data show quite different behaviours, as shown in Figure 2. BiCuSeO exhibits a moderate linear thermal expansion slope below 400 K, but deviates from this initial linear trend at higher temperatures, indicating a significant quartic contribution. On the other hand, Bi_2Te_3 shows overall larger linear thermal expansion due to the larger cubic anharmonicity below 400 K with only a small deviation from this linear trend at high temperature. Thus, while having the same overall Grüneisen parameter, Bi_2Te_3 and BiCuSeO have different relative contributions from cubic and quartic anharmonic contributions. We note that the thermoelectric figure-of-merit is enhanced across different temperature ranges in these materials, presumably due to differences in cubic and quartic anharmonic contributions. Bi_2Te_3 is used for thermoelectric applications at low temperatures, particularly below room temperatures, where its figure-of-merit is quite high [80], while BiCuSeO exhibits a large thermoelectric figure-of-merit at higher temperatures [16].

Finally, it is illuminating to compare our empirical study with the recent theoretical work on a measure of anharmonicity. Knoop and coworkers used the standard deviation (σ^A) of the distribution of anharmonic force components as a quantitative measure of anharmonicity in a material and provided a survey of a large number of materials [81]. The anharmonicity metric (σ^A) is extracted from ab initio molecular dynamics calculations and quantifies the magnitude of non-harmonic force components at a given temperature and volume. In contrast, the Grüneisen parameter γ is a thermodynamic quantity that captures the coupling between lattice vibrations and volume. As a result, γ and σ^A probes are related but not identical aspects of anharmonicity. Unfortunately, we found that only a small number of materials considered in our study are included in the list studied in Ref. [81], making a direct comparison difficult. With this caveat in mind, in Figure 4, we compare γ_0 determined from the XRD thermal expansion data reported here with σ^A_{MD} (T = 300 K) values from Ref. [81] for overlapping materials. While there is a clear positive correlation (linear regression $R \sim 0.8$), some outliers are notable. In particular, Knoop et al. found that σ^A_{MD} of cubic BN is smaller than that of hexagonal BN [81], which is opposite to the trend of γ_0. It will be interesting to expand the comparison between these theoretical and experimental estimates of lattice anharmonicity.

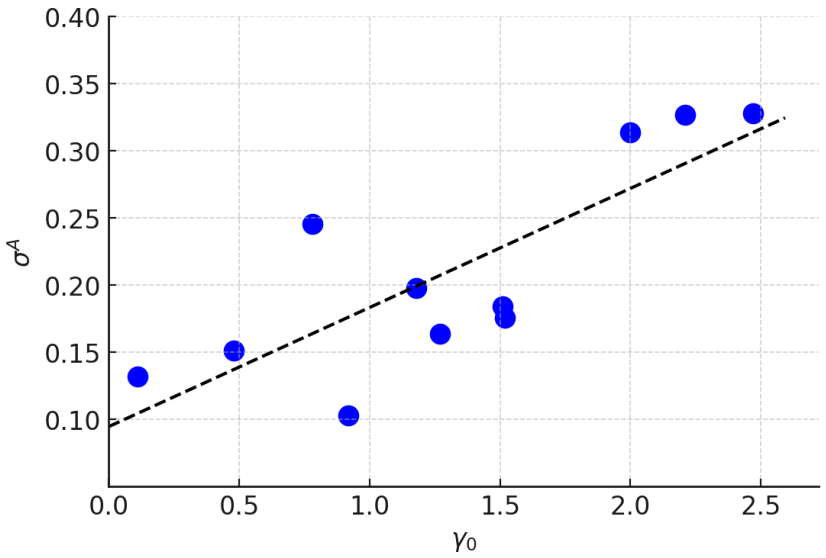


Figure 4. Comparison of experimentally determined γ_0 with σ^A_{MD} (T = 300 K) from Ref. [81]. From the smallest to the largest γ_0, these are h-BN, Si, ZnS, c-BN, CaO, BeO, MnO, MgO, PbTe, NaBr, and PbS. The dashed line is a linear regression fit.

Supplementary Materials: The following supporting information can be downloaded at: https://www.mdpi.com/article/10.3390/cryst16020118/s1, Table S1: Previous thermal expansion studies of the materials studied in this article from Ref. [82–92]; Table S2: Grüneisen parameter comparison data.

Author Contributions: Conceptualization, S.J. and Y.-J.K.; methodology, S.J. and A.C.; formal analysis, S.J. and A.C.; investigation, S.J. and A.C.; data curation, S.J.; writing—original draft preparation, S.J.; writing—review and editing, Y.-J.K.; visualization, S.J.; supervision, Y.-J.K.; funding acquisition, Y.-J.K. All authors have read and agreed to the published version of the manuscript.

Funding: This research was funded by the Natural Sciences and Engineering 303 Research Council (NSERC) of Canada [RGPIN-2019-06449; RTI-2019-00809; ALLRP 581160-22], Canada Foundation for Innovation [36404], and the Ontario Research Fund.

Data Availability Statement: The raw data supporting the conclusions of this article will be made available by the authors on request.

Acknowledgments: During the preparation of this manuscript, the authors used ChatGPT 5.0 to produce Figure 4 from the data collected by the authors. The authors have reviewed and edited the output and take full responsibility for the content of this publication.

Conflicts of Interest: The authors declare no conflicts of interest.

Appendix A. Thermal Average of Displacement

The statistical average of a thermodynamic quantity Q with thermal energy E would be [93]

$$\langle Q \rangle = \frac{\int Q e^{-\beta E}}{\int e^{-\beta E}} \tag{A1}$$

where $\beta = 1/(k_B T)$.

Substituting $Q = x$ and $E = \phi(x) = cx^2 - gx^3 - fx^4$ into this statistical average would yield Equation (3) in the main text:

$$\langle x \rangle_T = \frac{3}{4} g_1 a_r \epsilon [1 - G\epsilon - F\epsilon^2] \tag{A2}$$

Note that the product $g_1 a_r = g/c^2$, meaning that the obtained $\langle x \rangle_T$ is independent of a. Thus, it is simply quantified relative to the lattice constant a at a reference temperature T. For convenience, we take a_r and T_r to be the lowest experimental values and quantify thermal expansion as the increase from these values.

Since we are modelling thermal expansion over a wide temperature range, it is important to note that anharmonic deviations are more significant at higher temperatures. Thus, to capture these higher-temperature deviations, the model is geared towards higher-temperature approximations, such as the energy term $\epsilon \approx k_B T$ for simplicity. As shown by the fits, this simple model reproduces thermal expansion well across all temperatures.

Appendix B. Effective Potential Parameters

Fitting the thermal expansion data to Equation (4) in the main paper yields b_1, b_2, and b_3. Now, comparing to Equation (A2), we have

$$g_1 = \frac{4}{3}\frac{b_1}{k_B}, \; G = \frac{b_2}{k_B}, \; F = \frac{b_3}{k_B^2}$$

$$f_1 = \frac{2}{35}[\sqrt{G^2 + 4F} - G], \; g_2 = \frac{16}{15}\left[\frac{16\sqrt{G^2 + 4F} + 19G}{35}\right]$$

which finally yields

$$c = \frac{g_2}{(g_1 a_r)^2},\ g = c^2(g_1 a_r),\ f = f_1 c^2$$

Thus,

$$\begin{aligned} c &= \frac{3k_B}{5}\left[\frac{16\sqrt{b_2^2+4b_3}+19b_2}{35b_1^2a_r^2}\right] \\ g &= \frac{12k_B}{25}\left[\frac{\left(16\sqrt{b_2^2+4b_3}+19b_2\right)^2}{1225b_1^3a_r^3}\right] \\ f &= \frac{18k_B}{875}\left[\frac{\left(16\sqrt{b_2^2+4b_3}+19b_2\right)^2\left(\sqrt{b_2^2+4b_3}-b_2\right)}{1225b_1^4a_r^4}\right] \end{aligned} \tag{A3}$$

Appendix C. Grüneisen Parameter from Effective Potential

The Mie–Gruñeisen equation of state relates thermal pressure, P_T, with thermal energy, E_T:

$$P_T = \frac{\gamma E_T}{V} \tag{A4}$$

where V is the volume and γ is the Grüneisen parameter.

Considering atoms in a lattice, let an atom A be surrounded by n neighbouring atoms, each at a distance $A_n = a_n + u_n$, where a_n is the time-averaged component and u_n is the oscillatory component. Note that u_n allows for oscillations in all three dimensions. If the effective force experienced by atom A due to all these n neighbours is denoted by F_n, then the Cauchy stress tensor becomes

$$\tau = \frac{1}{2V}\sum_n a_n \langle F_n(a_n + u_n)\rangle \tag{A5}$$

Now, expanding the effective force up to a second-order approximation gives

$$F_n(a_n + u_n) \approx F_n(a_n) + F_n'(a_n)u_n + \frac{1}{2}F_n''(a_n)u_n^2$$

Substituting this back gives

$$\tau = \frac{1}{2V}\sum_n a_n F_n(a_n) + \frac{1}{4V}\sum_n a_n F_n''(a_n)\langle u_n^2\rangle,$$

since $\langle u_n\rangle = 0$, the thermal oscillation component.

Now, with $\tau = \tau_0 + \tau_T$, $P_T = tr(\tau_T)$ can be written as

$$P_T = \frac{1}{4V}\sum_n a_n F_n''(a_n)\langle u_n^2\rangle, \tag{A6}$$

where

$$F_n = -\frac{\partial \phi_n}{\partial x_n} = -\phi_n'$$

if we define a potential ϕ_n along a lattice direction (in one dimension) $a_n + x_n$.

Next, we have the potential energy as

$$U_T = \frac{1}{2}\sum_n \langle \phi_n(a_n + x_n) - \phi_n(a_n)\rangle$$

Expanding this effective potential up to the second order gives

$$\phi_n(a_n + x_n) \approx \phi_n(a_n) + \phi'_n(a_n).x_n + \frac{1}{2}\phi''_n(a_n).x_n^2$$

Substituting, this leads to

$$U_T = \frac{1}{4}\sum_n \phi''_n(a_n)\langle x_n^2\rangle.$$

By the equipartition theorem, or using the Virial theorem, the total energy would be

$$E_T = 2U_T = \frac{1}{2}\sum_n \phi''_n(a_n)\langle x_n^2\rangle \tag{A7}$$

Here, we make the crucial assumption that the thermal oscillations are only mediated by the first spherical coordination sphere. This allows us to replace the $\sum_n$ with the coordination number M, and in 3 dimensions,

$$\langle u_n^2\rangle = \frac{1}{3}\langle x_n^2\rangle.$$

Finally, substituting Equations (A6) and (A7) back in Equation (A4), we obtain Equation (5) of the main text:

$$\gamma_0 = -\frac{a}{6}\left[\frac{\phi'''(u)}{\phi''(u)}\right] \tag{A8}$$

References

1. Ashcroft, N.W.; Mermin, N.D. *Solid State Physics*; Holt, Rinehart and Winston: New York, NY, USA, 1976.
2. Chang, C.; Zhao, L.D. Anharmonicity and low thermal conductivity in thermoelectrics. *Mater. Today Phys.* **2018**, *4*, 50–57. [CrossRef]
3. Li, X.; Fauqué, B.; Zhu, Z.; Behnia, K. Phonon Thermal Hall Effect in Strontium Titanate. *Phys. Rev. Lett.* **2020**, *124*, 105901. [CrossRef]
4. He, X.; Bansal, D.; Winn, B.; Chi, S.; Boatner, L.; Delaire, O. Anharmonic Eigenvectors and Acoustic Phonon Disappearance in Quantum Paraelectric $SrTiO_3$. *Phys. Rev. Lett.* **2020**, *124*, 145901. [CrossRef] [PubMed]
5. Wang, Q.; Zeng, Z.; Chen, Y. Revisiting phonon transport in perovskite $SrTiO_3$: Anharmonic phonon renormalization and four-phonon scattering. *Phys. Rev. B* **2021**, *104*, 235205. [CrossRef]
6. Wu, Y.N.; Saidi, W.A.; Wuenschell, J.K.; Tadano, T.; Ohodnicki, P.; Chorpening, B.; Duan, Y. Anharmonicity Explains Temperature Renormalization Effects of the Band Gap in $SrTiO_3$. *J. Phys. Chem. Lett.* **2020**, *11*, 2518–2523. [CrossRef]
7. Martelli, V.; Jiménez, J.L.; Continentino, M.; Baggio-Saitovitch, E.; Behnia, K. Thermal Transport and Phonon Hydrodynamics in Strontium Titanate. *Phys. Rev. Lett.* **2018**, *120*, 125901. [CrossRef]
8. Mounet, N.; Marzari, N. First-principles determination of the structural, vibrational and thermodynamic properties of diamond, graphite, and derivatives. *Phys. Rev. B* **2005**, *71*, 205214. [CrossRef]
9. Cuffari, D.; Bongiorno, A. Calculation of Mode Grüneisen Parameters Made Simple. *Phys. Rev. Lett.* **2020**, *124*, 215501. [CrossRef]
10. Huang, L.F.; Lu, X.Z.; Tennessen, E.; Rondinelli, J.M. An efficient ab-initio quasiharmonic approach for the thermodynamics of solids. *Comp. Mater. Sci.* **2016**, *120*, 84–93. [CrossRef]
11. Liu, X.; Wang, H.; Wang, W.; Fu, Z. A prediction model of thermal expansion coefficient for cubic inorganic crystals by the bond valence model. *J. Solid State Chem.* **2021**, *299*, 122111. [CrossRef]
12. Xu, P.; Wang, H.; Ren, L.; Tu, B.; Wang, W.; Fu, Z. Theoretical study on composition-dependent properties of $ZnO{\cdot}nAl_2O_3$ spinels. Part II: Mechanical and thermophysical. *J. Am. Ceramic Soc.* **2021**, *104*, 6455–6466. [CrossRef]
13. Quareni, F.; Mulargia, F. The validity of the common approximate expressions for the Grüneisen parameter. *Geophys. J. Int.* **1988**, *93*, 505–519. [CrossRef]
14. Wan, C.L.; Pan, W.; Xu, Q.; Qin, Y.X.; Wang, J.D.; Qu, Z.X.; Fang, M.H. Effect of point defects on the thermal transport properties of $(La_xGd_{1-x})_2Zr_2O_7$: Experiment and theoretical model. *Phys. Rev. B* **2006**, *74*, 144109. [CrossRef]
15. Sanditov, D.S.; Belomestnykh, V.N. Relation between the parameters of the elasticity theory and averaged bulk modulus of solids. *Tech. Phys.* **2011**, *56*, 1619–1623. [CrossRef]

16. Pei, Y.L.; He, J.; Li, J.F.; Li, F.; Liu, Q.; Pan, W.; Barreteau, C.; Berardan, D.; Dragoe, N.; Zhao, L.D. Scaffolded biosensors with designed DNA nanostructures. *NPG Asia Mater.* **2013**, *5*, e51. [CrossRef]
17. Tranquada, J.M.; Ingalls, R. Extended X-ray—Absorption fine-structure study of anharmonicity in CuBr. *Phys. Rev. B* **1983**, *28*, 3520–3528. [CrossRef]
18. Stern, E.A.; Līvņš, P.; Zhang, Z. Thermal vibration and melting from a local perspective. *Phys. Rev. B* **1991**, *43*, 8850–8860. [CrossRef] [PubMed]
19. Dalba, G.; Fornasini, P.; Gotter, R.; Rocca, F. Anharmonicity effects on the extended X-ray-absorption fine structure: The case of β-AgI. *Phys. Rev. B* **1995**, *52*, 149–157. [CrossRef]
20. Hu, Y.; Salvador, J.R.; Chen, N.; Alatas, A.; Kim, Y.J. Anharmonicity in partially filled skutterudites $Yb_xCo_4Sb_{12}$. *J. Appl. Phys.* **2021**, *130*, 185105. [CrossRef]
21. Basu, R.; Nayak, C.; Kumar, R.; Bhattacharyya, D.; Jha, S.N.; Singh, A. Potency of Extended X-ray Absorption Fine Structure Spectroscopy toward the Determination of Individual Bond Grüneisen Parameter for High Thermoelectric Performance. *ACS Appl. Energy Mater* **2023**, *6*, 2981–2988. [CrossRef]
22. Knura, R.; Parashchuk, T.; Yoshiasa, A.; Wojciechowski, K.T. Origins of low lattice thermal conductivity of $Pb_{1-x}Sn_xTe$ alloys for thermoelectric applications. *Dalton Trans.* **2021**, *50*, 4323–4334. [CrossRef] [PubMed]
23. Mukherjee, G.D.; Bansal, C.; Chatterjee, A. Thermal Expansion Study of Ordered and Disordered Fe_3Al: An Effective Approach for the Determination of Vibrational Entropy. *Phys. Rev. Lett.* **1996**, *76*, 1876–1879. [CrossRef]
24. Hiramatsu, H.; Yanagi, H.; Kamiya, T.; Ueda, K.; Hirano, M.; Hosono, H. Crystal Structures, Optoelectronic Properties, and Electronic Structures of Layered Oxychalcogenides MCuOCh (M = Bi, La; Ch = S, Se, Te): Effects of Electronic Configurations of M^{3+} Ions. *Chem. Mater.* **2008**, *20*, 326–334. [CrossRef]
25. Radaelli, P.G.; Hinks, D.G.; Mitchell, A.W.; Hunter, B.A.; Wagner, J.L.; Dabrowski, B.; Vandervoort, K.G.; Viswanathan, H.K.; Jorgensen, J.D. Structural and superconducting properties of $La_{2-x}Sr_xCuO_4$ as a function of Sr content. *Phys. Rev. B* **1994**, *49*, 4163–4175. [CrossRef] [PubMed]
26. Cochran, W. *The Dynamics of Atoms in Crystals*; Edward Arnold (Publishers): London, UK, 1973; Chapter 8, p. 109.
27. Yoshiasa, A.; Okube, M.; Ohtaka, O.; Kamishima, O.; Katayama, Y. Anharmonic effective pair potentials of γ- and α-CuBr at high pressure. *Jpn. J. Appl. Phys.* **2000**, *39*, 6747–6751. [CrossRef]
28. Yoshiasa, A.; Okube, M.; Kamishima, O.; Arima, H.; Okudera, H.; Terada, Y.; Nakatsuka, A. Anharmonic effective pair potentials in α-, β-, and γ-CuI determined by extended X-ray absorption fine structure. *Solid State Ion.* **2005**, *176*, 2487–2491. [CrossRef]
29. Krivtsov, A.; Kuz'kin, V. Derivation of equations of state for ideal crystals of simple structure. *Mech. Solids* **2011**, *46*, 387. [CrossRef]
30. Minikayev, R.; Safari, F.; Katrusiak, A.; Szuszkiewicz, W.; Szczerbakow, A.; Bell, A.; Dynowska, E.; Paszkowicz, W. Thermostructural and Elastic Properties of PbTe and Pb0.884Cd0.116Te: A Combined Low-Temperature and High-Pressure X-ray Diffraction Study of Cd-Substitution Effects. *Crystals* **2021**, *11*, 1063. [CrossRef]
31. Zhang, Y.; Ke, X.; Chen, C.; Yang, J.; Kent, P.R.C. Thermodynamic properties of PbTe, PbSe, and PbS: First-principles study. *Phys. Rev. B* **2009**, *80*, 024304. [CrossRef]
32. Bessas, D.; Sergueev, I.; Wille, H.C.; Perßon, J.; Ebling, D.; Hermann, R.P. Lattice dynamics in Bi_2Te_3 and Sb_2Te_3: Te and Sb density of phonon states. *Phys. Rev. B* **2012**, *86*, 224301. [CrossRef]
33. Arafin, S.; Singh, R.N. Pressure variation of melting temperatures of alkali halides. *Int. J. Mod. Phys. B* **2017**, *31*, 1750031. [CrossRef]
34. Soma, T. Temperature Dependence of the Grüneisen Constant of Si and Ge. *Phys. Stat. Sol. B* **1977**, *82*, 319–324. [CrossRef]
35. Srivastava, S.P.; Srivastava, R.C.; Singh, I.D.; Pandey, S.D.; Gupta, P.L. Temperature Dependence of Thermal Expansion and Infrared Lattice Vibrational Mode of Nickel Oxide. *J. Phys. Soc. Jpn.* **1977**, *43*, 885–890. [CrossRef]
36. Kern, G.; Kresse, G.; Hafner, J. Ab initio calculation of the lattice dynamics and phase diagram of boron nitride. *Phys. Rev. B* **1999**, *59*, 8551–8559. [CrossRef]
37. Fanggao, C.; Cankurtaran, M.; Saunders, G.A.; Al-Kheffaji, A.; Almond, D.P.; Ford, P.J.; Ladds, D.A. Ultrasonic evidence of strong vibrational anharmonicity in high-Tc superconductors and its effect on determination of their elastic properties. *Phys. Rev. B* **1991**, *43*, 5526–5537. [CrossRef]
38. Fei, Y. Thermal Expansion. In *Mineral Physics & Crystallography*; American Geophysical Union (AGU): Washington, DC, USA, 1995; pp. 29–44. [CrossRef]
39. Schauer, A. Thermal expansion, Grueneisen parameter, and temperature dependence of lattice vibration frequencies of aluminum oxide. *Can. J. Phys.* **1965**, *43*, 523–531. [CrossRef]
40. Pei-Lun Lee, E.H.; Yu, S.C. Phase diagram and equations of state of $BaSO_4$. *High Press. Res.* **2001**, *21*, 67–77. [CrossRef]
41. Singh, J.; Sharma, V.K.; V., K.; Vaitheeswaran, G.; Errandonea, D. High-pressure structural, lattice dynamics, and electronic properties of beryllium aluminate studied from first-principles theory. *Mater. Today Commun.* **2021**, *26*, 101801. [CrossRef]

42. SOGA, N. Elastic Constants of Polycrystalline BeO as a Function of Pressure and Temperature. *J. Am. Chem. Soc.* **1969**, *52*, 246–249. [CrossRef]
43. Soga, N. Elastic properties of CaO under pressure and temperature. *J. Geophys. Res.* **1968**, *73*, 5385–5390. [CrossRef]
44. Saal, J.E.; Wang, Y.; Shang, S.; Liu, Z.K. Thermodynamic Properties of Co_3O_4 and $Sr_6Co_5O_{15}$ from First-Principles. *Inorg. Chem.* **2010**, *49*, 10291–10298. [CrossRef] [PubMed]
45. Dymshits, A.M.; Dorogokupets, P.I.; Sharygin, I.S.; Litasov, K.D.; Shatskiy, A.; Rashchenko, S.V.; Ohtani, E.; Suzuki, A.; Higo, Y. Thermoelastic properties of chromium oxide Cr_2O_3 (eskolaite) at high pressures and temperatures. *Phys. Chem. Miner.* **2016**, *43*, 447–458. [CrossRef]
46. Bruschini, E.; Speziale, S.; Bosi, F.; Andreozzi, G.B. Fe–Mg substitution in aluminate spinels: Effects on elastic properties investigated by Brillouin scattering. *Phys. Chem. Miner.* **2018**, *45*, 759–772. [CrossRef]
47. Campbell, A.J.; Danielson, L.; Righter, K.; Seagle, C.T.; Wang, Y.; Prakapenka, V.B. High pressure effects on the iron–iron oxide and nickel–nickel oxide oxygen fugacity buffers. *Earth Planet. Sci. Lett.* **2009**, *286*, 556–564. [CrossRef]
48. Jacobs, M.H.G.; van den Berg, A.P.; Schmid-Fetzer, R.; de Vries, J.; van Westrenen, W.; Zhao, Y. Thermodynamic properties of geikielite ($MgTiO_3$) and ilmenite ($FeTiO_3$) derived from vibrational methods combined with Raman and infrared spectroscopic data. *Phys. Chem. Miner.* **2022**, *49*, 23. [CrossRef]
49. Hoat, D.; Silva, J.R.; Blas, A. First principles study of structural, electronic, elastic and thermodynamic properties of cubic HfO_2 under pressure. *Phys. B Condens. Matter.* **2018**, *545*, 55–61. [CrossRef]
50. Hofmeister, A.; Mao, H. Pressure derivatives of shear and bulk moduli from the thermal Grüneisen parameter and volume-pressure data. *Geochim. Cosmochim. Acta* **2003**, *67*, 1215–1235. [CrossRef]
51. Yong, W.; Botis, S.; Shieh, S.R.; Shi, W.; Withers, A.C. Pressure-induced phase transition study of magnesiochromite ($MgCr_2O_4$) by Raman spectroscopy and X-ray diffraction. *Phys. Earth Planet. Inter.* **2012**, *196–197*, 75–82. [CrossRef]
52. Hunt, S.A.; Santangeli, J.R.; Dobson, D.P.; Wood, I.G. Phase diagram and thermal expansion of orthopyroxene-, clinopyroxene-, and ilmenite-structured $MgGeO_3$. *Am. Mineral.* **2021**, *106*, 1113–1127. [CrossRef]
53. Mitra, S. High-Pressure Geochemistry and Mineral Physics: Chapter 5 (Crystalline) Materials Under High Pressure. In *Developments in Geochemistry, Vol. 9*; Elsevier: Amsterdam, The Netherlands, 2004; pp. 401–511. [CrossRef]
54. Serizawa, H.; Arai, Y.; Suzuki, Y. Simultaneous determination of X-ray Debye temperature and Grüneisen constant for actinide dioxides: PuO_2 and ThO_2. *J. Nucl. Mater.* **2000**, *280*, 99–105. [CrossRef]
55. Arafin, S.; Singh, R.N. Thermal and physical properties of titanium oxide at high pressure. *J. Phys. Chem. Sol.* **2016**, *99*, 86–91. [CrossRef]
56. Goel, P.; Choudhury, N.; Chaplot, S. Atomistic modeling of the vibrational and thermodynamic properties of uranium dioxide, UO_2. *J. Nucl. Mater.* **2008**, *377*, 438–443. [CrossRef]
57. Wei, N.; Zhang, X.; Zhang, C.; Hou, S.; Zeng, Z. First-principles investigations on the elastic and thermodynamic properties of cubic ZrO_2 under high pressure. *Int. J. Mod. Phys. C* **2015**, *26*, 1550056. [CrossRef]
58. Soma, T. Thermal expansion and lattice dynamics under pressure of ZnS, ZnSe and ZnTe. *Solid State Commun.* **1980**, *34*, 927–932. [CrossRef]
59. Zhuravlev, Y.N.; Bugaeva, I.A.; Zhuravleva, L.V. Ab Initio Study of Thermodynamic Properties of Lithium, Sodium, and Potassium Sulfates. *Russ. Phys. J.* **2013**, *56*, 638–646. [CrossRef]
60. Hofmeister, A.; Mao, H. Evaluation of shear moduli and other properties of silicates with the spinel structure from IR spectroscopy. *Am. Mineral.* **2001**, *86*, 622–639. [CrossRef]
61. Zhang, Z.; Wentzcovitch, R.M. Ab initio anharmonic thermodynamic properties of cubic $CaSiO_3$ perovskite. *Phys. Rev. B* **2021**, *103*, 104108. [CrossRef]
62. Kulik, E.; Murzin, V.; Kawaguchi, S.; Nishiyama, N.; Katsura, T. Thermal expansion of coesite determined by synchrotron powder X-ray diffraction. *Phys. Chem. Miner.* **2018**, *45*, 873–881. [CrossRef]
63. Barron, T.H.K.; Collins, J.F.; Smith, T.W.; White, G.K. Thermal expansion, Gruneisen functions and static lattice properties of quartz. *J. Phys. C Solid State Phys.* **1982**, *15*, 4311. [CrossRef]
64. Graham, E.K. On the Compression of Stishovite. *Geophys. J. Int.* **1973**, *32*, 15–34. [CrossRef]
65. HIRAO, K.; SOGA, N. Heat capacity and Grueneisen parameter of alkali aluminosilicate glasses. *J. Ceram. Soc. Jpn.* **1982**, *90*, 476–481. [CrossRef]
66. Sanditov, D.S.; Mashanov, A.A.; Darmaev, M.V.; Sanditov, B.D.; Mantatov, V.V. Grüneisen parameter and elastic constants of crystals and vitreous bodies. *Russ. Phys. J.* **2009**, *52*, 221–230. [CrossRef]
67. Singh, P. Equation of state and thermoelastic properties of Mg_2SiO_4. *Comput. Condens. Matter* **2022**, *31*, e00678. [CrossRef]
68. Ehlers, A.M.; Zaffiro, G.; Angel, R.J.; Boffa-Ballaran, T.; Carpenter, M.A.; Alvaro, M.; Ross, N.L. Thermoelastic properties of zircon: Implications for geothermobarometry. *Am. Mineral.* **2022**, *107*, 74–81. [CrossRef]
69. Knight, K.S. Low-temperature thermophysical and crystallographic properties of $BaZrO_3$ perovskite. *J. Mater. Sci.* **2020**, *55*, 6417–6428. [CrossRef]

70. Liu, W.; Kung, J.; Wang, L.; Li, B. Thermal equation of state of $CaGeO_3$ perovskite. *Am. Mineral.* **2008**, *93*, 745–750. [CrossRef]
71. Kung, J.; Rigden, S.M.; Jackson, I. Silicate perovskite analogue $ScAlO_3$: Temperature dependence of elastic moduli. *Phys. Earth Planet. Inter.* **2000**, *120*, 299–314. [CrossRef]
72. Knight, K.S.; Bull, C.L. Low temperature and high pressure thermoelastic and crystallographic properties of SrZrO3 perovskite in the Pbnm phase. *Solid State Sci.* **2016**, *62*, 90–104. [CrossRef]
73. Zhang, L.; Liu, M.; Ren, W.; Zhou, Z.; Dong, G.; Zhang, Y.; Peng, B.; Hao, X.; Wang, C.; Jiang, Z.D.; et al. ALD preparation of high-k HfO_2 thin films with enhanced energy density and efficient electrostatic energy storage. *RSC Adv.* **2017**, *7*, 8388–8393. [CrossRef]
74. Liu, J.; Li, J.; Wu, J.; Sun, J. Structure and Dielectric Property of High-k ZrO_2 Films Grown by Atomic Layer Deposition Using Tetrakis(Dimethylamido)Zirconium and Ozone. *Nanoscale Res. Lett.* **2019**, *14*, 154. [CrossRef]
75. Saleh, R.H.; Deeb, M. Study of electrical properties of cobalt oxide-doped sodium meta vanadate at different frequencies. *Heliyon* **2022**, *8*. [CrossRef]
76. Young, K.F.; Frederikse, H.P.R. Compilation of the Static Dielectric Constant of Inorganic Solids. *J. Phys. Chem. Ref. Data* **1973**, *2*, 313–410. [CrossRef]
77. Strand, J.W.; Cottom, J.; Larcher, L.; Shluger, A.L. Effect of electric field on defect generation and migration in HfO_2. *Phys. Rev. B* **2020**, *102*, 014106. [CrossRef]
78. Wilk, G.D.; Wallace, R.M.; Anthony, J.M. High-κ gate dielectrics: Current status and materials properties considerations. *J. Appl. Phys.* **2001**, *89*, 5243–5275. [CrossRef]
79. Wang, Y.; Chen, Z.; Shi, T.; Moritz, B.; Shen, Z.X.; Devereaux, T.P. Phonon-Mediated Long-Range Attractive Interaction in One-Dimensional Cuprates. *Phys. Rev. Lett.* **2021**, *127*, 197003. [CrossRef] [PubMed]
80. Goldsmid, H.J. Bismuth Telluride and Its Alloys as Materials for Thermoelectric Generation. *Materials* **2014**, *7*, 2577–2592. [CrossRef]
81. Knoop, F.; Purcell, T.A.R.; Scheffler, M.; Carbogno, C. Anharmonicity measure for materials. *Phys. Rev. Mater.* **2020**, *4*, 083809. [CrossRef]
82. Vaqueiro, P.; Al Orabi, R.A.R.; Luu, S.D.N.; Guélou, G.; Powell, A.V.; Smith, R.I.; Song, J.P.; Wee, D.; Fornari, M. The role of copper in the thermal conductivity of thermoelectric oxychalcogenides: Do lone pairs matter? *Phys. Chem. Chem. Phys.* **2015**, *17*, 31735–31740. [CrossRef]
83. Kastbjerg, S.; Bindzus, N.; Søndergaard, M.; Johnsen, S.; Lock, N.; Christensen, M.; Takata, M.; Spackman, M.A.; Brummerstedt Iversen, B. Direct Evidence of Cation Disorder in Thermoelectric Lead Chalcogenides PbTe and PbS. *Adv. Funct. Mater.* **2013**, *23*, 5477–5483. [CrossRef]
84. Božin, E.S.; Malliakas, C.D.; Souvatzis, P.; Proffen, T.; Spaldin, N.A.; Kanatzidis, M.G.; Billinge, S.J.L. Entropically Stabilized Local Dipole Formation in Lead Chalcogenides. *Science* **2010**, *330*, 1660–1663. [CrossRef]
85. Pavlova, L.M.; Shtern, Y.I.; Mironov, R.E. Thermal Expansion of Bismuth Telluride. *High Temp.* **2011**, *49*, 369. [CrossRef]
86. Shen, Y.; Saunders, C.N.; Bernal, C.M.; Abernathy, D.L.; Manley, M.E.; Fultz, B. Anharmonic Origin of the Giant Thermal Expansion of NaBr. *Phys. Rev. Lett.* **2020**, *125*, 085504. [CrossRef]
87. Rao, A.; Narender, K.; Rao, K.; Krishna, N. Thermophysical Properties of NaCl, NaBr and NaF by γ-Ray Attenuation Technique. *J. Mod. Phys.* **2013**, *4*, 208–214. [CrossRef]
88. Okada, Y.; Tokumaru, Y. Precise determination of lattice parameter and thermal expansion coefficient of silicon between 300 and 1500 K. *J. Appl. Phys.* **1984**, *56*, 314–320. [CrossRef]
89. Solozhenko, V.; Peun, T. Compression and thermal expansion of hexagonal graphite-like boron nitride up to 7 GPa and 1800 K. *J. Phys. Chem. Solids* **1997**, *58*, 1321–1323. [CrossRef]
90. Chen, J.; Xu, X.; Yuan, B.; Deng, J.; Xing, X. Thermal expansion of cubic boron nitride. *Acta Metall. Sin.* **2003**, *39*, 952.
91. Ding Yu, J.; Inaguma, Y.; Itoh, M.; Oguni, M.; Kyômen, T. Effect of oxygen content on the anomalies at successive phase transitions of $La_2CuO_{4+\delta}$ single crystal below 320 K. *Phys. Rev. B* **1996**, *54*, 7455–7461. [CrossRef] [PubMed]
92. Ono, Y.O.Y.; ya Narita Shin-ya Narita, S. Anomalous Thermal Expansion in $La_{2-x}Sr_xCuO_4$. *Jpn. J. Appl. Phys.* **1992**, *31*, L224. [CrossRef]
93. Kittel, C. *Introduction to Solid State Physics*; John Wiley & Sons: New York, NY, USA, 2004.

Disclaimer/Publisher's Note: The statements, opinions and data contained in all publications are solely those of the individual author(s) and contributor(s) and not of MDPI and/or the editor(s). MDPI and/or the editor(s) disclaim responsibility for any injury to people or property resulting from any ideas, methods, instructions or products referred to in the content.